Geometrically nonlinear finite element model for predicting failure in composite structures

M. Patni[a,*], S. Minera[a], C. Bisagni[b], P.M. Weaver[a,c], A. Pirrera[a]

[a] *Bristol Composites Institute (ACCIS), Department of Aerospace Engineering, University of Bristol, Queen's Building, University Walk, Bristol BS8 1TR, UK.*
[b] *Aerospace Structures and Computational Mechanics, Faculty of Aerospace Engineering, Delft University of Technology, 2629 HS, Delft, Netherlands.*
[c] *Bernal Institute, School of Engineering, University of Limerick, Castletroy, Ireland.*

Abstract

Composite structures are extensively used in many industries, where they are subjected to a variety of loads and may undergo large deformations. Reliable utilisation of such structures requires prior knowledge of their failure response. In order to predict failure loads and modes, accurate, yet computationally efficient, evaluation of three-dimensional (3D) stress fields becomes important. In this paper, we present a modelling approach, based on the Unified Formulation, that accounts for geometric nonlinearity in laminated composites and predicts 3D stress fields for subsequent failure analysis. The approach builds upon the hierarchical Serendipity Lagrange finite elements and is able to capture high-order shear deformation, as well as local cross-sectional warping. A total Lagrangian approach is adopted and the classic Newton-Raphson method is employed to solve the nonlinear governing equations. A key novelty of the proposed formulation is its completeness and its applicability to fully anisotropic structures. In other words, using the Green-Lagrange strain components within the Unified Formulation framework, the explicit form of the tangent stiffness matrix is derived including general stiffness properties. This new model is benchmarked against 3D finite element solution, as well as other formulations available in the literature, by means of static analyses of highly nonlinear, laminated composite beam-like structures. Significant computational efficiency gains over 3D finite elements are observed for similar levels of accuracy. Furthermore, to show the enhanced capabilities of the present formulation, the postbuckling response of a composite stiffened panel is compared with experimental results from the literature. The 3D stress fields computed in the postbuckling regime are used to detect failure of the stiffened panel. The corresponding failure mode, as obtained by the new model, is shown to match with the experiment.

Keywords: Large Deflection; Finite Element; Composite Stiffened Panel; Failure Initiation.

1. Introduction

As environmental concerns and governmental regulations push towards a more efficient use of materials and resources, engineering structures are progressively being developed and optimised to, *e.g.*, reduce their mass and/or increase their performance and fuel efficiency. Composite materials offer considerable advantages in the impetus towards lightweighting, due to their high specific stiffness and strength. In combination, these more stringent design drivers and the availability of advanced materials promote the employment of increasingly slender and thin-walled, monocoque and semi-monocoque structures. The aerospace, automotive and wind energy industries provide prime examples of structures that gain efficiency through increased slenderness. See, for instance, the A350 and 787 wings or recent multi-MW wind turbine blades. However, as slenderness increases, structures become more susceptible to complex nonlinear deformations. Engineers

*Corresponding author: mayank.patni@bristol.ac.uk

must, therefore, be aware of the limits of both elastic stability and material strength to produce efficient, reliable designs. For instance, composite stiffened panels, commonly used in aerospace structures, can, in many cases, operate far beyond the buckling load and only fail deep into the postbuckling range [1]. In order to account for such failures, accurate prediction of the structural behaviour, including failure mechanisms, is essential during, and possibly early into, the design phase.

In this regard, significant efforts have been made in the development of tools for predicting ply failure mechanisms under plane stress states [2–4]. However, using two-dimensional (2D) stress fields in conjunction with 2D failure theories may not result in accurate evaluation of the failure indices, and thus, three-dimensional (3D) stress states are required [5]. In general, predicting 3D stress fields accurately in composite structures is important as through-thickness damage, such as delamination, is driven by transverse shear and transverse normal stresses. Moreover, using 3D stress states in a consistent way, provides not only the prediction for the onset of ply damage, but also additional information regarding the type of failure and the orientation of the fracture plane [6, 7]. To this end, high-fidelity finite element methods (FEM) are often employed to obtain reliable 3D stresses with the desired level of accuracy [8]. However, using these models becomes prohibitively expensive, from a computational standpoint, whenever thin and/or multi-layered composite structures are to be analyzed. The problem is further exacerbated for the already costly geometrically nonlinear or transient analyses. Although many efforts have been carried out over recent decades with numerous numerical models being proposed to assess the nonlinear structural response of laminated composites [9–13], perhaps due to the computational cost and complexity, the reporting of fully 3D nonlinear stress analyses of laminates in the literature is rather limited.

Of relevance to the present work, a recent contribution to the field of structural mechanics is the Unified Formulation (UF) by Carrera and co-workers [14, 15]. The formulation extends the kinematics of one-dimensional (beam) and two-dimensional (plate and shell) models over the cross-section (beam case) and through the thickness (plate and shell cases) by employing various expansion functions. The available literature shows the UF's capability to solve a wide range of structural mechanics problems in an efficient manner. de Miguel *et al.* [16] performed failure evaluations using 3D stress fields determined by employing Lagrange expansions. The approach is shown to be computationally efficient compared to 3D Finite Element (FE) models and also computes accurate out-of-plane stress fields required for predicting the onset of delamination in multi-layered composites. However, de Miguel's work is limited to linear static analyses. In recent works by Pagani and Carrera [17, 18], the UF is extended to account for large deflections and postbuckling of solid and thin-walled laminated beam structures. Global/local deformations were investigated using Lagrange expansion functions in the cross-section. The model is limited to monoclinic material and is not suitable for analysing anisotropic material structures. More recently, in order to capture shear deformations and local cross-sectional warping, Hui *et al.* [19] proposed a geometrically nonlinear high-order kinematic model using hierarchical expansion functions (Taylor) in the cross-section. Although, the model predicts the displacement and stress fields accurately and efficiently, it is based on a plane-stress assumption, and therefore, cannot capture 3D stress fields. Moreover, more general limitations of using the Taylor-expansion-based Unified Formulation are highlighted in [20].

As an alternative approach, we propose to employ the Serendipity Lagrange Expansion (SLE) elements previously developed by the authors in [20]. The model, combines two of the main features of the Taylor and the Lagrange expansion elements, *i.e.* it is hierarchical and allows for numerically stable cross-sectional refinements via re-meshing. The model was developed with an aim to capture localised 3D stress fields near geometric features, and was recently extended to account for constant- and variable-stiffness laminated composite structures [21–23]. In the present paper, we aim to further extend the formulation to deal with large displacements and nonlinear kinematics. To do so, the total Lagrangian approach is used and the tangent stiffness matrix of the element is derived from the weak form of the governing equations obtained via the Principle of Virtual Displacement. For the first time in the nonlinear UF framework, all terms of the material stiffness matrix are considered to account for general anisotropy. Furthermore, the explicit form of the tangent stiffness matrix is given in a novel concise form, which simplifies its algorithmic implementation. The second Piola-Kirchhoff stresses employed by the total Lagrangian formulation are transformed into true Cauchy's stresses, which are physically meaningful. The model so-developed is benchmarked against numerical and experimental results by means of static and failure analyses of nonlinear, laminated composite

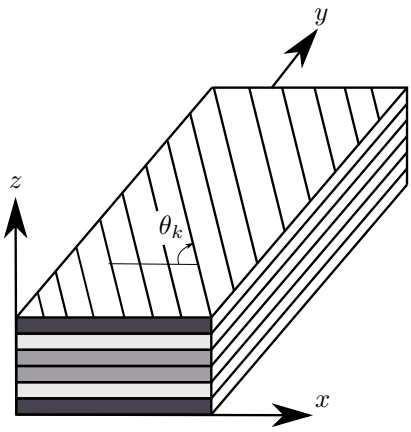

Figure 1: Reference system for a laminated beam.

structures.

The remainder of the paper is structured as follows. Section 2.1 and 2.2 provides preliminary and introductory information on the Unified Formulation framework, including Green-Lagrange nonlinear geometrical relations and elastic constitutive equations. In Section 2.3, the tangent stiffness matrix is presented explicitly, followed by a discussion on computing co-rotational Cauchy's stresses in Section 2.4. In Section 3, the efficacy of the proposed nonlinear model is shown by means of large deflection analyses of various structures. The solutions obtained are compared with numerical and experimental results. Finally, conclusions are drawn in Section 4.

2. Mathematical Formulation

2.1. Preliminaries

Consider a laminated beam of length L and rectangular cross-section of width b and thickness h, composed of N_l layers. The material properties and the thickness of each layer may be entirely different. The beam is referred to a Cartesian coordinate system (x,y,z), where the y-direction is defined to be along the principal beam axis, while the z-axis is in the transverse stacking direction as shown in Figure 1. Let θ denote the fibre orientation and the subscript k be used to refer to the k^{th} layer. For points in the structure's volume, the three-dimensional displacement field is given as

$$\boldsymbol{U}(x,y,z) = \{u \quad v \quad w\}^\top, \tag{1}$$

and the displacement gradient vector $\boldsymbol{\Phi}$ can be written as

$$\boldsymbol{\Phi} = \{u_{,x} \quad u_{,y} \quad u_{,z} \quad v_{,x} \quad v_{,y} \quad v_{,z} \quad w_{,x} \quad w_{,y} \quad w_{,z}\}^\top, \tag{2}$$

where a subscript preceded by a comma denotes differentiation with respect to the corresponding spatial coordinate.

To account for large deformations, the Green-Lagrange strain vector $\boldsymbol{E}$ is considered, which is given by

$$\boldsymbol{E} = \left[\boldsymbol{H} + \frac{1}{2}\boldsymbol{A}\right]\boldsymbol{\Phi}, \tag{3}$$

and the virtual variation of the Green-Lagrange strain vector [24] is given by

$$\delta\boldsymbol{E} = \delta\left\{\left[\boldsymbol{H} + \frac{1}{2}\boldsymbol{A}\right]\boldsymbol{\Phi}\right\} = [\boldsymbol{H} + \boldsymbol{A}]\,\delta\boldsymbol{\Phi}, \tag{4}$$

where

$$\boldsymbol{E} = \{E_{xx} \quad E_{yy} \quad E_{zz} \quad E_{yz} \quad E_{xz} \quad E_{xy}\}^\top,$$

$$\boldsymbol{H} = \begin{bmatrix} 1 & 0 & 0 & 0 & 0 & 0 & 0 & 0 & 0 \\ 0 & 0 & 0 & 0 & 1 & 0 & 0 & 0 & 0 \\ 0 & 0 & 0 & 0 & 0 & 0 & 0 & 0 & 1 \\ 0 & 0 & 0 & 0 & 0 & 1 & 0 & 1 & 0 \\ 0 & 0 & 1 & 0 & 0 & 0 & 1 & 0 & 0 \\ 0 & 1 & 0 & 1 & 0 & 0 & 0 & 0 & 0 \end{bmatrix},$$

$$\boldsymbol{A} = \begin{bmatrix} u_{,x} & 0 & 0 & v_{,x} & 0 & 0 & w_{,x} & 0 & 0 \\ 0 & u_{,y} & 0 & 0 & v_{,y} & 0 & 0 & w_{,y} & 0 \\ 0 & 0 & u_{,z} & 0 & 0 & v_{,z} & 0 & 0 & w_{,z} \\ 0 & u_{,z} & u_{,y} & 0 & v_{,z} & v_{,y} & 0 & w_{,z} & w_{,y} \\ u_{,z} & 0 & u_{,x} & v_{,z} & 0 & v_{,x} & w_{,z} & 0 & w_{,x} \\ u_{,y} & u_{,x} & 0 & v_{,y} & v_{,x} & 0 & w_{,y} & w_{,x} & 0 \end{bmatrix}.$$

In the present work, the material is assumed to undergo deformation within the linear elastic range and, therefore, Hooke's law provides the constitutive relation at layer level:

$$\boldsymbol{S} = \bar{\boldsymbol{C}}\boldsymbol{E}, \tag{5}$$

where $\boldsymbol{S} = \{S_{xx} \quad S_{yy} \quad S_{zz} \quad S_{yz} \quad S_{xz} \quad S_{xy}\}^\top$ is the second Piola-Kirchhoff stress tensor and $\bar{\boldsymbol{C}}$ is the transformed material stiffness matrix expressed in the global Cartesian coordinate system,

$$\bar{\boldsymbol{C}} = \begin{bmatrix} \bar{C}_{11} & \bar{C}_{12} & \bar{C}_{13} & \bar{C}_{14} & \bar{C}_{15} & \bar{C}_{16} \\ & \bar{C}_{22} & \bar{C}_{23} & \bar{C}_{24} & \bar{C}_{25} & \bar{C}_{26} \\ & & \bar{C}_{33} & \bar{C}_{34} & \bar{C}_{35} & \bar{C}_{36} \\ & & & \bar{C}_{44} & \bar{C}_{45} & \bar{C}_{46} \\ & \textit{Symmetric} & & & \bar{C}_{55} & \bar{C}_{56} \\ & & & & & \bar{C}_{66} \end{bmatrix}. \tag{6}$$

The coefficients $\bar{C}_{ij}$ relate to the elastic coefficients in material coordinates, C_{ij}, via the transformation matrix $\boldsymbol{Q}$, whose elements are obtained from the direction cosines of the material coordinate system projected onto the global x, y, z coordinate directions. Specifically,

$$\bar{\boldsymbol{C}} = \boldsymbol{Q}\boldsymbol{C}\boldsymbol{Q}^\top. \tag{7}$$

The coefficients C_{ij} and the matrix $\boldsymbol{Q}$ are not included here for sake of brevity, but can be found in Section 5.4 of [25].

2.2. Serendipity-Lagrange-based nonlinear Finite Element Model

Our model employs the Unified Formulation framework, where a 3D structure is discretised with a finite number of transverse planes running along the principal axis of the structure. For simplicity, this axis can be thought of as a beam axis and the transverse planes as the beam's cross-sections. The Unified Formulation [14, 15] relies on a displacement-based version of the finite element method. In the current setting, the longitudinal axis of the structure is discretised with N_e-noded, 1D finite elements, so that the displacement field can be approximated element-wise by means of local shape functions, $N_i(y)$. In addition, the transverse, or cross-sectional deformations, are approximated using hierarchical Serendipity Lagrange expansion (SLE) functions, $F_\tau(x,z)$ [20], such that

$$\boldsymbol{U}(x,y,z) = \sum_{i=1}^{N_\mathrm{e}} \sum_{\tau=1}^{m} N_i(y) F_\tau(x,z) \boldsymbol{U}_{i\tau}. \tag{8}$$

where m is the number of terms depending on the order of SL expansion, and $\boldsymbol{U}_{i\tau}$ are generalised three-dimensional displacement vectors.

Adopting this expansion model, cross-sections are discretised using four-noded Lagrange sub-domains (SLE nodes). The displacement field within each sub-domain can be enriched by increasing the order of the local Serendipity Lagrange expansion. This model allows a layer-wise approach to be implemented directly by using a sub-domain for each layer. In addition, the kinematics within each layer (or sub-domain) can be varied hierarchically. The reader is referred to [20, 21] for a more detailed implementation and treatment of SLE models.

For the sake of clarity, it is important to stress that, using Eq. (8), the cross-sectional mesh (indicated by discretisation variable τ) captures the warping of the cross-section with one set of 2D shape functions ($F_\tau(x,z)$), while the axial behaviour is modelled by a separate 1D mesh (indicated by discretisation variable i) with an independent set of 1D shape functions ($N_i(y)$). This approach differentiates the method from classic 3D FEM, where 3D shape functions are used over volumetric brick or tetrahedral elements that offer no separation of cross-sectional and axial deformations. Moreover, the current methodology overcomes the limitation on the aspect ratio of a 3D brick element in FE analysis by decoupling the shape functions along the longitudinal axis and across the transverse plane.

By substituting Eq. (8) in Eq. (2), the displacement gradient vector can be written as

$$\boldsymbol{\Phi} = \boldsymbol{G}_{i\tau}\boldsymbol{U}_{i\tau} \tag{9}$$

where

$$\boldsymbol{G}_{i\tau} = \begin{bmatrix} N_i F_{\tau,x} & 0 & 0 \\ N_{i,y} F_\tau & 0 & 0 \\ N_i F_{\tau,z} & 0 & 0 \\ 0 & N_i F_{\tau,x} & 0 \\ 0 & N_{i,y} F_\tau & 0 \\ 0 & N_i F_{\tau,z} & 0 \\ 0 & 0 & N_i F_{\tau,x} \\ 0 & 0 & N_{i,y} F_\tau \\ 0 & 0 & N_i F_{\tau,z} \end{bmatrix}, \quad \boldsymbol{U}_{i\tau} = \begin{Bmatrix} u_{i\tau} \\ v_{i\tau} \\ w_{i\tau} \end{Bmatrix}.$$

In the previous expression and throughout remainder of the paper, the Einstein summation convention is implied over repeated indices.

Elastic equilibrium is enforced via the Principle of Virtual Displacements, by equating the internal and external virtual work, δW_{int} and δW_{ext}. By definition, the internal work is the work done by the internal stresses over the corresponding internal strains and is equivalent to the elastic strain energy. Noting that $W_{\text{int}} = \sum_{\text{e}} W^{\text{e}}_{\text{int}}$, where $W^{\text{e}}_{\text{int}}$ represents the strain energy per element and V^{e} be the volume of the generic element in an undeformed state,

$$\delta W^{\text{e}}_{\text{int}} = \int_{V^{\text{e}}} \delta \boldsymbol{E}^{\top} \boldsymbol{S}\, dV. \tag{10}$$

In the notation of the Unified Formulation [20], the internal work can be re-written as

$$\delta W^{\text{e}}_{\text{int}} = \delta \boldsymbol{U}^{\top}_{js} \boldsymbol{K}^{\tau sij}_{\text{s}} \boldsymbol{U}_{i\tau}, \tag{11}$$

where the term $\boldsymbol{K}^{\tau sij}_{\text{s}}$ is referred to as the *Fundamental Nuclei* of the secant stiffness matrix. Its explicit form for an orthotropic lamina can be found in [18]. Fundamental nuclei are assembled into a global stiffness matrix following the standard finite element procedure. For the sake of brevity, the derivation of the fundamental nucleus of the loading vector from the virtual variation of the external work is not reported here, but can be found in [15]. In the present work, we employ the full Newton-Raphson method to solve the nonlinear governing equations. The main disadvantage of using the secant stiffness matrix as in Eq. (11) would be its low convergence rate. Moreover, the secant matrix is not uniquely defined and is generally non-symmetric [18]. Therefore, in the following section, we derive the tangent stiffness matrix, as a more suitable alternative for the Newton-Raphson iterative solver employed herein.

2.3. Fundamental Nucleus of the Tangent Stiffness Matrix

In the present work, a classical Newton iteration method [26] is employed to solve the nonlinear system, which requires formulation of the tangent stiffness matrix. The fundamental nucleus of the tangent stiffness matrix is obtained from the linearisation of the virtual variation of the strain energy [18] as follows

$$d(\delta W_{\text{int}}^{\text{e}}) = \int_{V^{\text{e}}} d(\delta \boldsymbol{E}^{\top} \boldsymbol{S})\, dV = \int_{V^{\text{e}}} \delta \boldsymbol{E}^{\top} d\boldsymbol{S}\, dV + \int_{V^{\text{e}}} d(\delta \boldsymbol{E}^{\top}) \boldsymbol{S}\, dV. \tag{12}$$

The first term requires the linearisation of the constitutive relation (Eq. (5)), which, under the assumption of constant material stiffness and following Eq. (4), can be recast as

$$\int_{V^{\text{e}}} \delta \boldsymbol{E}^{\top} d\boldsymbol{S}\, dV = \int_{V^{\text{e}}} \left(\delta \boldsymbol{\Phi}^{\top} \Big\{ [\boldsymbol{H} + \boldsymbol{A}]^{\top} \bar{\boldsymbol{C}}\, [\boldsymbol{H} + \boldsymbol{A}] \Big\} d\boldsymbol{\Phi} \right) dV. \tag{13}$$

The second term requires the linearisation of the virtual variation of the Green-Lagrange strain vector, which, after manipulation [24], can be written in the following form:

$$\int_{V^{\text{e}}} d(\delta \boldsymbol{E}^{\top}) \boldsymbol{S}\, dV = \int_{V^{\text{e}}} \delta \boldsymbol{\Phi}^{\top} \hat{\boldsymbol{S}} d\boldsymbol{\Phi}\, dV, \tag{14}$$

where

$$\hat{\boldsymbol{S}} = \begin{bmatrix} S_{xx} & S_{xy} & S_{xz} & 0 & 0 & 0 & 0 & 0 & 0 \\ S_{xy} & S_{yy} & S_{yz} & 0 & 0 & 0 & 0 & 0 & 0 \\ S_{xz} & S_{yz} & S_{zz} & 0 & 0 & 0 & 0 & 0 & 0 \\ 0 & 0 & 0 & S_{xx} & S_{xy} & S_{xz} & 0 & 0 & 0 \\ 0 & 0 & 0 & S_{xy} & S_{yy} & S_{yz} & 0 & 0 & 0 \\ 0 & 0 & 0 & S_{xz} & S_{yz} & S_{zz} & 0 & 0 & 0 \\ 0 & 0 & 0 & 0 & 0 & 0 & S_{xx} & S_{xy} & S_{xz} \\ 0 & 0 & 0 & 0 & 0 & 0 & S_{xy} & S_{yy} & S_{yz} \\ 0 & 0 & 0 & 0 & 0 & 0 & S_{xz} & S_{yz} & S_{zz} \end{bmatrix}.$$

Substituting Eqs. (9), (13) and (14) into (12), the linearised version of the virtual variation of the strain energy is written as

$$\begin{aligned} d(\delta W_{\text{int}}^{\text{e}}) &= \delta \boldsymbol{U}_{js}^{\top} \left(\int_{V^{\text{e}}} \boldsymbol{G}_{js}^{\top} \Big\{ [\boldsymbol{H}^{\top} + \boldsymbol{A}^{\top}]\, \bar{\boldsymbol{C}}\, [\boldsymbol{H} + \boldsymbol{A}] + \hat{\boldsymbol{S}} \Big\} \boldsymbol{G}_{i\tau}\, dV \right) d\boldsymbol{U}_{i\tau}, \\ &= \delta \boldsymbol{U}_{js}^{\top} \left(\boldsymbol{K}_{\text{ll}}^{\tau s i j} + \boldsymbol{K}_{\text{l nl}}^{\tau s i j} + \boldsymbol{K}_{\text{nl l}}^{\tau s i j} + \boldsymbol{K}_{\text{nl nl}}^{\tau s i j} + \boldsymbol{K}_{\sigma}^{\tau s i j} \right) d\boldsymbol{U}_{i\tau}, \\ &= \delta \boldsymbol{U}_{js}^{\top}\, \boldsymbol{K}_{\text{T}}^{\tau s i j}\, d\boldsymbol{U}_{i\tau}, \end{aligned} \tag{15}$$

where $\boldsymbol{K}_{\text{T}}^{\tau s i j}$ is the fundamental nucleus of the tangent stiffness matrix, which, in turn, is composed of a linear term, $\boldsymbol{K}_{\text{ll}}^{\tau s i j}$, the nonlinear terms, $\boldsymbol{K}_{\text{l nl}}^{\tau s i j}$, $\boldsymbol{K}_{\text{nl l}}^{\tau s i j}$ and $\boldsymbol{K}_{\text{nl nl}}^{\tau s i j}$, and the geometric stiffness term, $\boldsymbol{K}_{\sigma}^{\tau s i j}$, where these are defined as follows:

$$\begin{aligned} \boldsymbol{K}_{\text{ll}}^{\tau s i j} &= \int_{V^{\text{e}}} \boldsymbol{G}_{js}^{\top} \boldsymbol{H}^{\top} \bar{\boldsymbol{C}} \boldsymbol{H} \boldsymbol{G}_{i\tau}\, dV, \\ \boldsymbol{K}_{\text{l nl}}^{\tau s i j} &= \int_{V^{\text{e}}} \boldsymbol{G}_{js}^{\top} \boldsymbol{H}^{\top} \bar{\boldsymbol{C}} \boldsymbol{A} \boldsymbol{G}_{i\tau}\, dV, \\ \boldsymbol{K}_{\text{nl l}}^{\tau s i j} &= \int_{V^{\text{e}}} \boldsymbol{G}_{js}^{\top} \boldsymbol{A}^{\top} \bar{\boldsymbol{C}} \boldsymbol{H} \boldsymbol{G}_{i\tau}\, dV, \\ \boldsymbol{K}_{\text{nl nl}}^{\tau s i j} &= \int_{V^{\text{e}}} \boldsymbol{G}_{js}^{\top} \boldsymbol{A}^{\top} \bar{\boldsymbol{C}} \boldsymbol{A} \boldsymbol{G}_{i\tau}\, dV, \\ \boldsymbol{K}_{\sigma}^{\tau s i j} &= \int_{V^{\text{e}}} \boldsymbol{G}_{js}^{\top} \hat{\boldsymbol{S}} \boldsymbol{G}_{i\tau}\, dV. \end{aligned} \tag{16}$$

These matrices are of size 3×3 for given i, j, τ, s and can be computed for each $\tau, s = 1, \ldots, m$, and $i, j = 1, \ldots, N_e$, in order to obtain the elemental tangent stiffness matrix for beam models of any order. Once the elemental tangent stiffness matrix is obtained, it is assembled into a global stiffness matrix following the standard finite element procedure.

In the present work, geometrically nonlinear stiffness terms, accounting for fully anisotropic material properties, are presented for the first time in the Unified Formulation framework. Therefore, for the sake of completeness, giving the explicit form of all nine components of the tangent stiffness matrix, for each of the nucleus sub-matrices, is important. However, each term in the fundamental nucleus involves summing a large number of expressions. Writing these long expressions is cumbersome and it also increases the chance of introducing a typing error while programming. For instance, each $\boldsymbol{K}_{ll}^{\tau sij}$ term requires summation of 9 expressions as follows:

$$\begin{aligned}\boldsymbol{K}_{ll}^{\tau sij}(1,1) = &\int_V \bar{C}_{11} F_{\tau,x} F_{s,x} N_i N_j dV + \int_V \bar{C}_{16} F_{\tau,x} F_s N_i N_{j,y} dV + \int_V \bar{C}_{15} F_{\tau,x} F_{s,z} N_i N_j dV \\ &+ \int_V \bar{C}_{16} F_\tau F_{s,x} N_{i,y} N_j dV + \int_V \bar{C}_{66} F_\tau F_s N_{i,y} N_{j,y} dV + \int_V \bar{C}_{56} F_\tau F_{s,z} N_{i,y} N_j dV \\ &+ \int_V \bar{C}_{15} F_{\tau,z} F_{s,x} N_i N_j dV + \int_V \bar{C}_{56} F_{\tau,z} F_s N_i N_{j,y} dV + \int_V \bar{C}_{55} F_{\tau,z} F_{s,z} N_i N_j dV.\end{aligned} \tag{17}$$

Similarly, $\boldsymbol{K}_{l\,nl}^{\tau sij}$ and $\boldsymbol{K}_{nl\,l}^{\tau sij}$ terms require 27 expressions each, while $\boldsymbol{K}_{nl\,nl}^{\tau sij}$ terms require 81 expressions. Furthermore, these matrices are of size 3×3 and non-symmetric, which increases the above count by a multiple of 9.

To overcome this complication, we devised an algorithmic and simplified way of writing the expressions in a concise form using Einstein's summation notation over repeated indices:

$$\begin{aligned}\boldsymbol{K}_{ll}^{\tau sij}(\alpha,\beta) &= < \bar{C}_{\alpha b \beta a} (N_i F_\tau)_{,a} (N_j F_s)_{,b} >, \\ \boldsymbol{K}_{l\,nl}^{\tau sij}(\alpha,\beta) &= < \bar{C}_{\alpha b a c} (N_i F_\tau)_{,a} (N_j F_s)_{,b} (N_l F_p)_{,c} > \boldsymbol{U}_{lp}(\beta), \\ \boldsymbol{K}_{nl\,l}^{\tau sij}(\alpha,\beta) &= < \bar{C}_{\beta a b c} (N_i F_\tau)_{,a} (N_j F_s)_{,b} (N_m F_q)_{,c} > \boldsymbol{U}_{mq}(\alpha), \\ \boldsymbol{K}_{nl\,nl}^{\tau sij}(\alpha,\beta) &= < \bar{C}_{acbd} (N_i F_\tau)_{,a} (N_j F_s)_{,b} (N_l F_p)_{,c} (N_m F_q)_{,d} > \boldsymbol{U}_{lp}(\beta) \boldsymbol{U}_{mq}(\alpha), \\ \boldsymbol{K}_{\sigma}^{\tau sij}(\alpha,\beta) &= \begin{cases} \boldsymbol{k}_{\sigma}^{\tau sij}(1,1) + \boldsymbol{k}_{\sigma}^{\tau sij}(2,2) + \boldsymbol{k}_{\sigma}^{\tau sij}(3,3) & \text{for} \quad \alpha = \beta \\ 0 & \text{for} \quad \alpha \neq \beta \end{cases},\end{aligned} \tag{18}$$

with

$$\begin{aligned}\boldsymbol{k}_{\sigma}^{\tau sij}(\alpha,\alpha) = &< \bar{C}_{\alpha c a b} (N_i F_\tau)_{,a} (N_j F_s)_{,b} (N_l F_p)_{,c} > \boldsymbol{U}_{lp}(\alpha) \\ &+ \frac{1}{2} < \bar{C}_{abcd} (N_i F_\tau)_{,a} (N_j F_s)_{,b} (N_l F_p)_{,c} (N_m F_q)_{,d} > \boldsymbol{U}_{lp}(\alpha) \boldsymbol{U}_{mq}(\alpha),\end{aligned} \tag{19}$$

where $\alpha, \beta = 1, 2, 3$, are row and column indices; $a, b, c, d = 1, 2, 3$, unless preceded by a comma denoting differentiation, in which case $a, b, c, d = x, y, z$; $< (.) >$ denotes $\int_V (.)\, dV$, which is evaluated numerically by employing Gauss Quadrature; and where $\bar{\boldsymbol{C}}$ is expressed as a fourth-order tensor (cf. Eq.(6)), as

$$\bar{\boldsymbol{C}} = \begin{bmatrix} \bar{C}_{1111} & \bar{C}_{1122} & \bar{C}_{1133} & \bar{C}_{1123} & \bar{C}_{1113} & \bar{C}_{1112} \\ & \bar{C}_{2222} & \bar{C}_{2233} & \bar{C}_{2223} & \bar{C}_{2213} & \bar{C}_{2212} \\ & & \bar{C}_{3333} & \bar{C}_{3323} & \bar{C}_{3313} & \bar{C}_{3312} \\ & & & \bar{C}_{2323} & \bar{C}_{2313} & \bar{C}_{2312} \\ & \textit{symmetric} & & & \bar{C}_{1313} & \bar{C}_{1312} \\ & & & & & \bar{C}_{1212} \end{bmatrix}. \tag{20}$$

This concise way not only reduces the task, but also speeds up the computation process by natural vectorisation of the loop. Finally, it is to be noted that the expressions are independent of the type of expansion function used in the cross-section.

2.4. Corotational Cauchy Stress

The Cauchy stress tensor $\boldsymbol{\sigma}$ is derived from the Second-Piola stress tensor $\boldsymbol{S}$ using the deformation gradient $\boldsymbol{F}$. Specifically,

$$\boldsymbol{\sigma} = \frac{1}{\det F}\,\boldsymbol{F}\boldsymbol{S}\boldsymbol{F}^{\top}, \tag{21}$$

where

$$\boldsymbol{F} = \begin{bmatrix} 1+u_{,x} & u_{,y} & u_{,z} \\ v_{,x} & 1+v_{,y} & v_{,z} \\ w_{,x} & w_{,y} & 1+w_{,z} \end{bmatrix}. \tag{22}$$

The Cauchy stress tensor is referenced in the global coordinate system, which does not have a clear physical meaning in case of large deformations. Therefore, corotational Cauchy stresses are computed on the deformed configuration using the rotation tensor, $\boldsymbol{R}$:

$$\hat{\boldsymbol{\sigma}} = \boldsymbol{R}^{\top}\boldsymbol{\sigma}\boldsymbol{R}. \tag{23}$$

The rotation tensor $\boldsymbol{R}$ is obtained by polar decomposition of the deformation gradient as per [27].

3. Numerical Results

In this section, to demonstrate the capabilities of the proposed geometrically nonlinear Unified Formulation, based on Serendipity Lagrange expansions (UF-SLE), various benchmark problems are addressed. The first example presents the large deflection analysis of an isotropic cantilever beam in bending. In the second, highly flexible, laminated composite plate strips are considered and their nonlinear responses are compared with 3D FE solutions and other numerical results available in the literature. In both cases, attention focuses on highlighting the ability of the UF-SLE model to account for complex nonlinear 3D stress states. In the third example, the postbuckling response of a single-stringer panel under axial compression is compared with experimental results from the literature. The 3D stress analysis capabilities of the present model are exploited for predicting the onset of failure in the panel.

3.1. Isotropic Beam

Consider a clamped-free, square cross-section beam of length $L = 1$ m, height and width $h = b = 0.05$ m, subjected to a bending load, P_z, applied at the free end ($y = L$), as shown in Figure 2. The Young's modulus, E, and Poisson's ratio, ν, of the constituent material, which is isotropic, are 2.9 GPa and 0.33, respectively. The non-dimensional quantities

$$\bar{u}_z = \frac{u_z}{L}, \qquad \bar{u}_y = \frac{u_y}{L}, \qquad \bar{P} = \frac{P_z L^2}{EI}, \tag{24}$$

are defined as metrics to benchmark the results, where u_z indicates vertical deflection, u_y indicates axial deflection and I is the second moment of area of the square cross-section.

In the present UF-SLE model, the beam structure is discretised using 20 B4 (four-noded cubic Lagrange) elements along its length and 1 SL5 (fifth-order Serendipity Lagrange) element in the cross-section. A 3D FE analysis, performed with commercial finite element software `ANSYS`, is used as a reference for validation, where the beam is discretised using 10,000 SOLID186 (3D 20-noded) elements to yield converged results. With the proposed model convergence is achieved with 4,209 degrees of freedom (DOFs), whereas in case of `ANSYS`, 139,623 DOFs are required. Figure 3 shows the normalised load-deflection curve, where the vertical and axial deflection components, $\bar{u}_z$ and $\bar{u}_y$, are measured at the centre of the tip of the beam. In addition to the 3D FE solution, exact analytical solution given by Bisshopp and Drucker [28], and experimental results obtained by Kemper [29], are used to validate the UF-SLE model. From the plots, it is evident that the nonlinear equilibrium curve obtained using the UF-SLE model is in excellent agreement with the 3D FE solution. The curves slightly differ with the analytical solution, but a better correlation is observed with the experimental results.

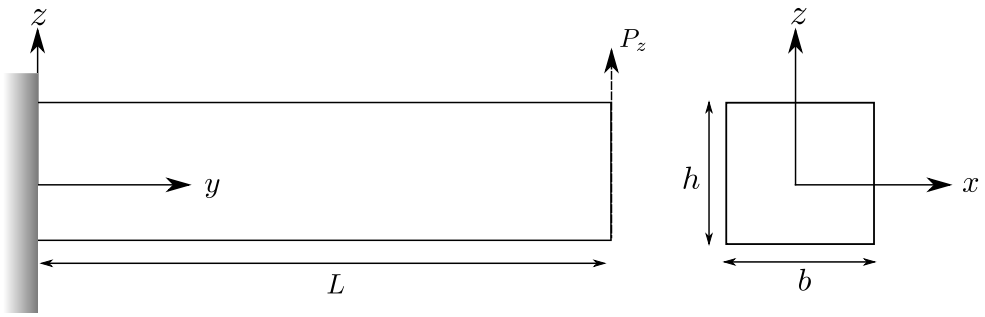

Figure 2: Square cross-section cantilever beam with applied tip load.

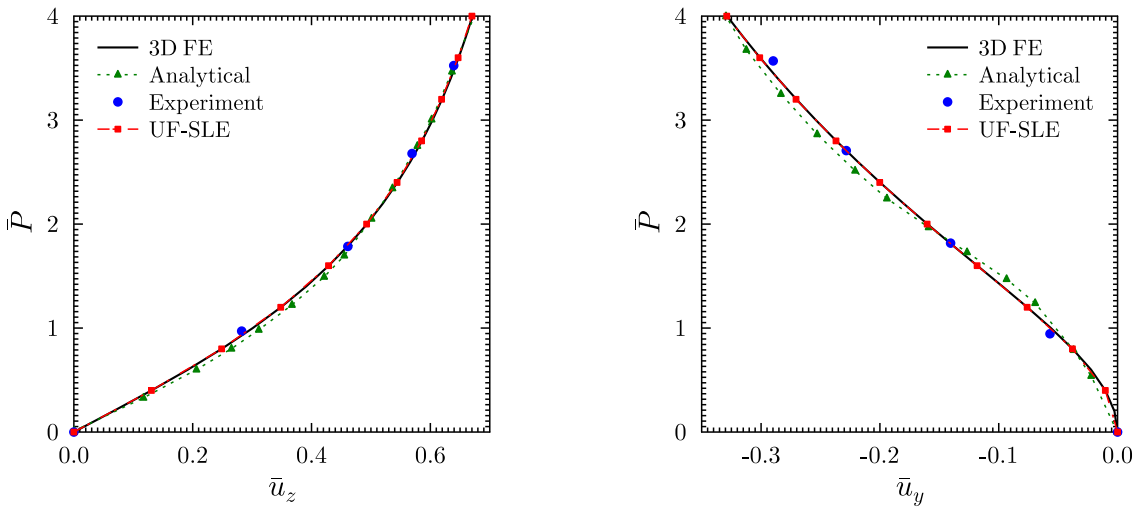

(a) $\bar{P}$ vs $\bar{u}_z$ curve at $(0, L, 0)$

(b) $\bar{P}$ vs $\bar{u}_y$ curve at $(0, L, 0)$

Figure 3: Load-deflection curve at the tip centre of a square cross-section isotropic beam. Analytical and experimental results are taken from [28] and [29], respectively.

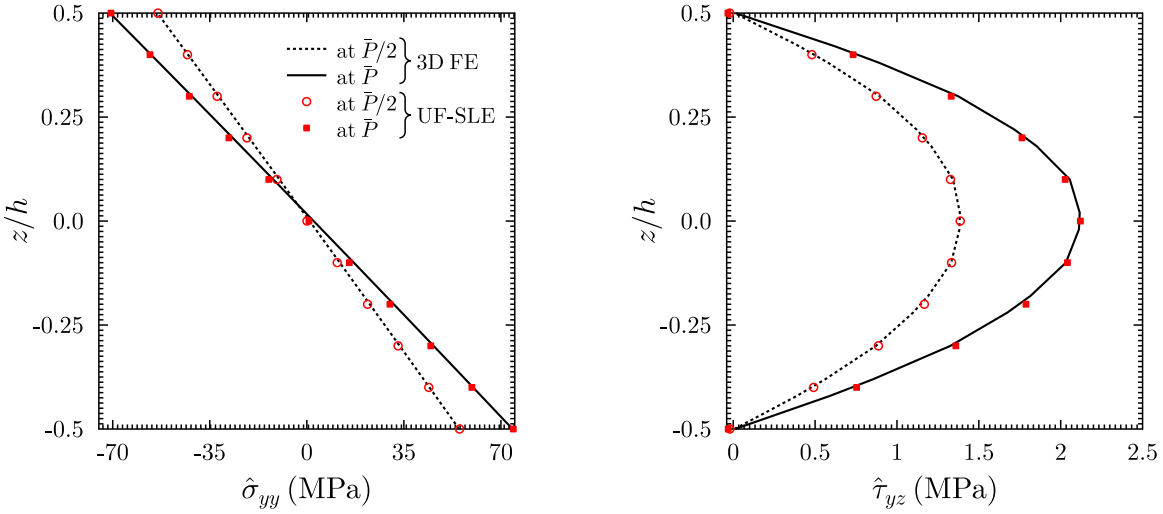

(a) $\hat{\sigma}_{yy}$ at $(0, L/2, z)$

(b) $\hat{\tau}_{yz}$ at $(0, L/2, z)$

Figure 4: Through-thickness distribution of the axial normal and transverse shear stresses at beam's mid-span for two load steps, $\bar{P}/2$ and $\bar{P}$.

Furthermore, to show the capability of the model in capturing stresses accurately, the through-thickness distribution of the axial normal, $\hat{\sigma}_{yy}$, and transverse shear, $\hat{\tau}_{yz}$, stresses, at two different load steps ($\bar{P}/2$ and $\bar{P}$), are shown in Figure 4. The stress results obtained are compared with the 3D FE solution. The nonlinear UF-SLE model, which employs the three-dimensional Green-Lagrange strain/displacement relation within a total Lagrangian approach, is able to replicate the 3D FE model with a limited number of DOFs.

3.2. Thin Composite Plate Strip

In this section, a multi-layered composite plate strip is considered, as shown in Figure 5. The length, width and thickness of the strip are $L = 10$ m, $b = 1$ m and $h = 0.1$ m, respectively. The plate strip is clamped at the end $y = 0$ and is subjected to a bending load, $P_z = 5\ N$, applied uniformly across the section at the end $y = L$. The material properties of the orthotropic laminae, considered herein are:

$E_x = 0.3$ MPa	$E_y = 1$ MPa	$E_z = 0.3$ MPa
$G_{yz} = 0.15$ MPa	$G_{xz} = 0.12$ MPa	$G_{xy} = 0.15$ MPa
$\nu_{yz} = 0.25$	$\nu_{xz} = 0.25$	$\nu_{xy} = 0.075$.

Four different layups are used: [0/90/0], [90/0/90], [-45/45/-45/45], [30/-60/-60/30]. In order to decide the number of beam and cross-section elements employed in the UF-SLE model, a mesh convergence analysis was performed. For converged deflection and normal stress responses, 40 B4 elements along the y-direction and 1 SL5 (fifth-order expansion) element per layer in the cross-section proved sufficient. However, higher fidelity is required for nonlinear transverse shear stresses and, therefore, 3 SL8 (eighth order expansion) elements per layer were required for the cross-section. For the sake of brevity, only converged results are presented here.

The nonlinear load-deflection curve (P_z vs u_z) at the plate's tip centre $(0, L, 0)$, for the different lamination schemes, is plotted in Figure 6. The present results are compared with those obtained by performing a 3D FE analysis in ANSYS and also with the reference solution given by Payette & Reddy [30] using a seven-parameter, spectral/hp shell finite element. As expected, the stacking sequence [90/0/90] is the most flexible while [0/90/0] is the most stiff, out of all of the stacking sequences analysed herein.

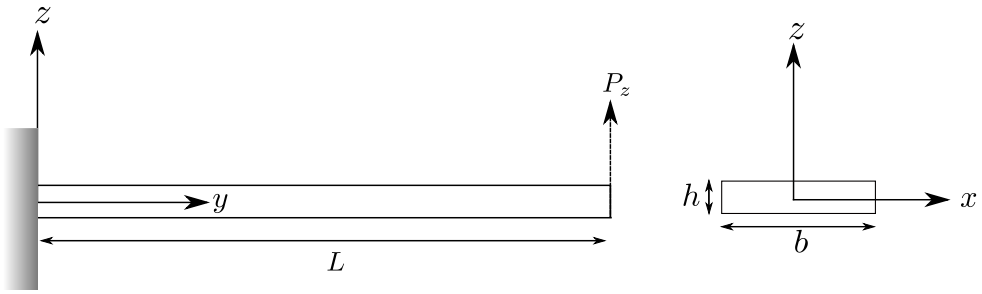

Figure 5: Thin plate strip subjected to a bending load

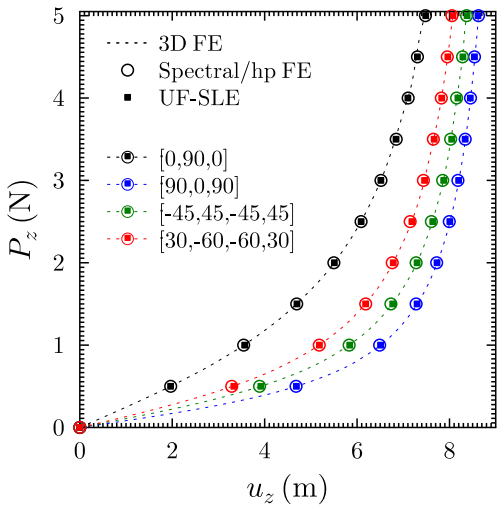

Figure 6: Load-deflection curve at the tip centre $(0, L, 0)$ of laminated plate strips. Spectral/hp FE results are taken from [30].

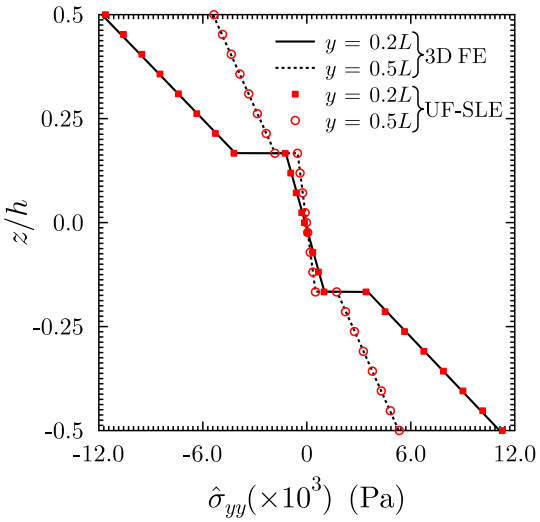

(a) $\hat{\sigma}_{yy}$ at $(0, L/5, z)$ and $(0, L/2, z)$

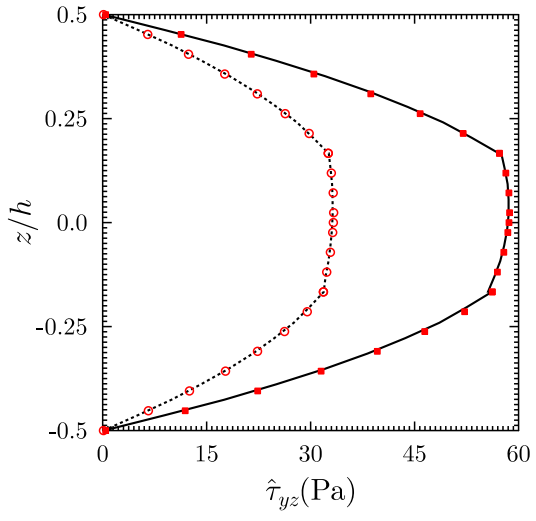

(b) $\hat{\tau}_{yz}$ at $(0, L/5, z)$ and $(0, L/2, z)$

Figure 7: Through-thickness distribution of the axial normal and transverse shear stresses at $y = 0.2L$ and $0.5L$, measured from the clamped end, for composite plate strip with layup [0/90/0].

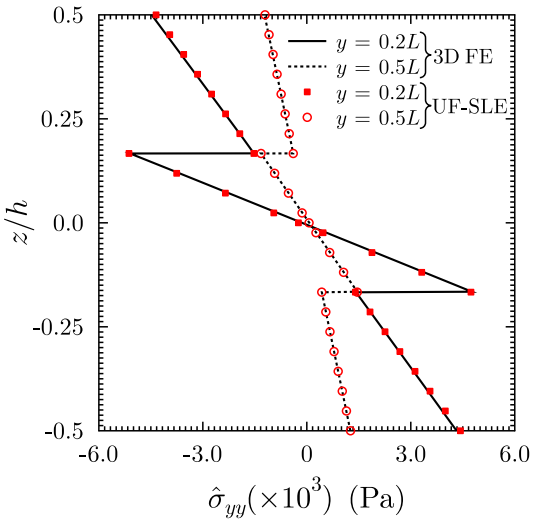

(a) $\hat{\sigma}_{yy}$ at $(0, L/5, z)$ and $(0, L/2, z)$

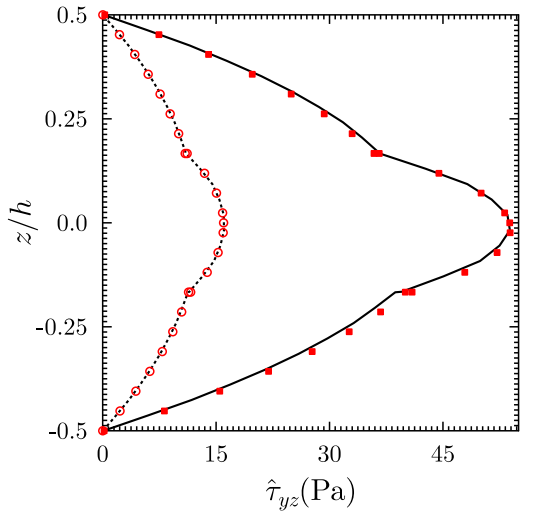

(b) $\hat{\tau}_{yz}$ at $(0, L/5, z)$ and $(0, L/2, z)$

Figure 8: Through-thickness distribution of the axial normal and transverse shear stresses at $y = 0.2L$ and $0.5L$, measured from the clamped end, for composite plate strip with layup [90/0/90].

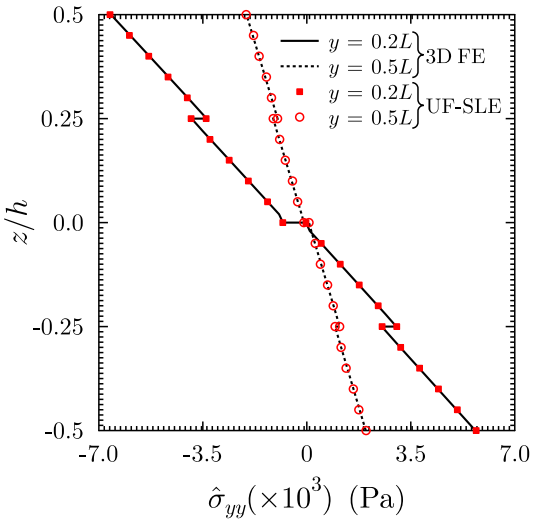

(a) $\hat{\sigma}_{yy}$ at $(0, L/5, z)$ and $(0, L/2, z)$

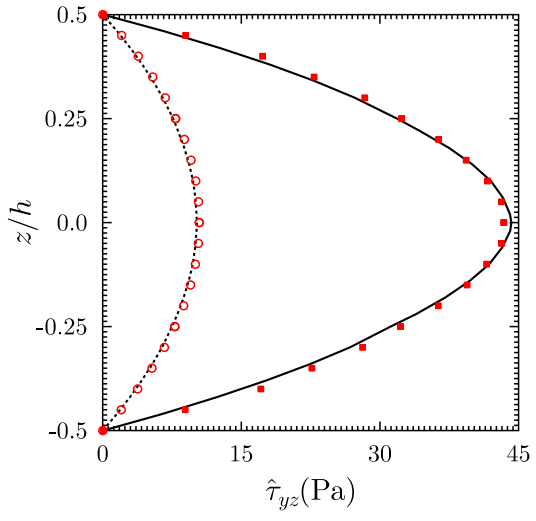

(b) $\hat{\tau}_{yz}$ at $(0, L/5, z)$ and $(0, L/2, z)$

Figure 9: Through-thickness distribution of the axial normal and transverse shear stresses at $y = 0.2L$ and $0.5L$, measured from the clamped end, for composite plate strip with layup [-45/45/-45/45].

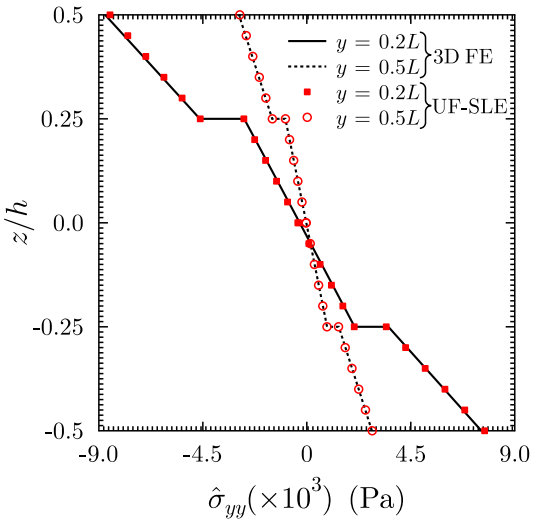

(a) $\hat{\sigma}_{yy}$ at $(0, L/5, z)$ and $(0, L/2, z)$

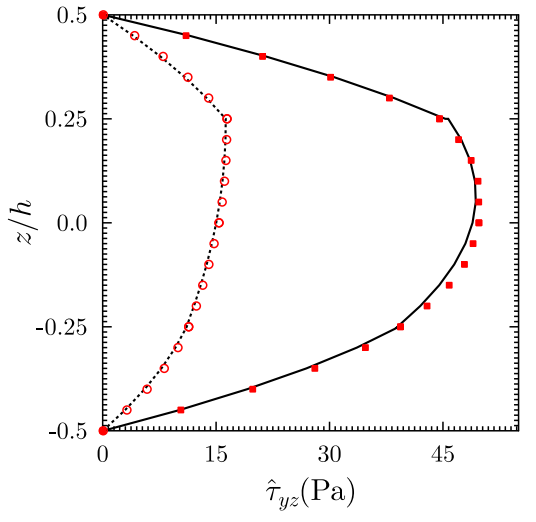

(b) $\hat{\tau}_{yz}$ at $(0, L/5, z)$ and $(0, L/2, z)$

Figure 10: Through-thickness distribution of the axial normal and transverse shear stresses at $y = 0.2L$ and $0.5L$, measured from the clamped end, for composite plate strip with layup [30/-60/-60/30].

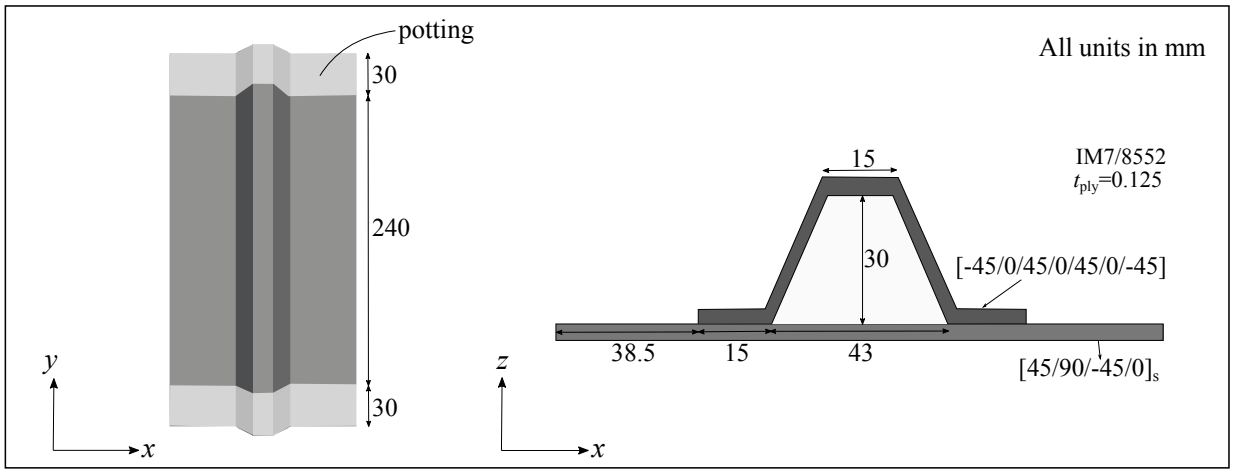

Figure 11: Single-stringer composite stiffened panel: configuration and dimensions.

From the load-deflection curve (Figure 6), it is evident that the examples considered in this section behave nonlinearly. Solving large-deflection problems can be cumbersome, especially if accurate stress fields are to be measured. In order to test the suitability of the UF-SLE model for predicting the nonlinear stress response accurately, the predicted distributions of axial normal stress, $\hat{\sigma}_{yy}$, and transverse shear stress, $\hat{\tau}_{yz}$, are compared with 3D FE solutions. figs. 7 to 10 show an excellent agreement between the two models, where the through-thickness stress distribution, computed at two different locations along the structure's length ($y = 0.2L$ and $0.5L$), are plotted for all the layups considered herein. The benefit of using the UF-SLE model is the ability to tune its fidelity by changing the order of expansion, as opposite to remeshing. As mentioned previously, to obtain the stress response of figs. 7 to 10, an eighth order expansion model is employed. This high-order model is computationally expensive (with ∼0.15 million DOFs), but it is still preferable to the `ANSYS` solution, which requires 102,000 20-noded brick elements and ∼1.3 million DOFs.

3.3. Composite Stiffened Panel

In this section, the proposed geometrically nonlinear UF-SLE model is employed for predicting the onset of failure in a single-stringer composite panel subjected to compression. This example is adapted from the work done by Bisagni *et al.* [1, 31, 32], where experimental tests were conducted on single-stringer compression (SSC) specimens and a shell-based FE model with damage capabilities was developed to predict the panel's postbuckling response, and the damage evolution from initiation to collapse. In the present study, the UF-SLE model is assessed by evaluating its performance in predicting the postbuckling response of the SSC specimen. Moreover, the model's capability to evaluate 3D stress fields accurately is exploited for predicting damage initiation.

The geometrical configuration and dimensions of the single-stringer hat specimen are shown in Figure 11. Both the skin and the stringer are made from IM7/8552 graphite-epoxy material, with mechanical properties and strength values as shown in Tables 1 and 2, respectively. The skin consists of an 8-ply quasi-isotropic laminate with a stacking sequence of $[45/90/-45/0]_s$, resulting in the total thickness of 1 mm. The stringer comprises of 7 plies with symmetric stacking sequence $[-45/0/45/0/45/0/-45]$, which results in a total thickness of 0.875 mm. The displacement constraints imposed at the two ends of the SSC specimen, using potting (by means of two 30 mm long tabs cast), ensure a uniform distribution of the load during the experiment [31]. To mimic this condition in the UF-SLE model, all the nodes within the potting region (refer to Figure 11) are fixed at one end (between $y = 0$ and $y = 30$ mm) and are allowed to move only in the longitudinal direction at the opposite end (between $y = 270$ mm and $y = 300$ mm). The specimen is subjected to a uniformly distributed compressive load $P = 41$ kN, applied to the end $y = 300$ mm.

To obtain the nonlinear static response of the SSC specimen, in the UF-SLE model, the cross-section is discretised with 195 SL5 (fifth-order expansion) elements, while 10 B4 elements are employed in the

Table 1: Mechanical properties of the IM7/8552 composite [33].

E_x	E_y	E_z	G_{yz}	G_{xz}	G_{xy}	ν_{yz}	ν_{xz}	ν_{xy}
(GPa)								
9.08	150	9.08	5.6	2.8	5.6	0.32	0.5	0.019

Table 2: Material strength values (in MPa) of the IM7/8552 composite [33].

Intralaminar							Interlaminar	
ST_{11}	SC_{11}	ST_{22}	SC_{22}	SS_{12}	SS_{13}	SS_{23}	ST_{33}	SS_{33}
2560	1590	73	185	90	90	57	63	90

longitudinal direction. This discretisation and cross-sectional expansion results in a total of 234,825 DOFs, which guaranty convergence. Figure 12 shows the load-displacement curve obtained with the UF-SLE model, which agrees well with the shell-based FE solution. The structural response is also compared with the experimental results. It can be seen that the experimental load-displacement curve exhibits softer behaviour than the numerical predictions. As discussed in [31], one possible reason for this behaviour could be the nonlinearity of the compression modulus E_y, which is not taken into account in either numerical model. Another reason for this discrepancy could be the difference between the specimen's actual and predicted stiffness values, as the compressive stiffness and strength of carbon composites are notoriously difficult to measure and length-scale dependent.

For further comparison and verification of the present modelling approach, Figure 13 shows the out-of-plane displacement response at different load levels. Up to an applied load of 2 kN (Point A), the structure exhibits a quasi-linear response with a single-wave out-of-plane deformation of the skin. The first buckling load (Point B) corresponds to a three half-wave mode and affects the skin only. The buckling load is predicted to be 7.8 kN by the UF-SLE model and 7.5 kN by the shell model (see [31]). Progressing with the UF-SLE model to the load level of 24.5 kN (Point C), shallow buckles become visible on the two webs of the stringer. This load corresponds to stringer buckling. Similar out-of plane deformation with the shell FE model is observed at 23.5 kN. Upon further loading, at 39.5 kN, the out-of-plane displacements are maximum. This load triggers failure initiation. Figure 13e shows the comparison of the predicted and measured deformation shapes immediately before collapse. It is observed that the number of half-waves in both the skin and the stringer, as predicted by the UF-SLE model, correlates well with the experimental observation and the shell FE solution.

Figure 14a and 14b show the crippling and delamination modes of failure in the test specimen. The crippling of the stringer is characterised by a fracture that travels across the stringer width. Different modes of crippling of the stringer were obtained for different specimens. Figure 14a shows a specimen in which the fracture is oriented at 45° in the crown and in the webs, and at 90° in the flanges. Whereas, the specimen shown in Figure 14b exhibits a fracture at approximately the mid-length of the specimen that runs across the stringer at a 90° angle. In most of the specimens, fibre pullouts were identified at various locations along the stringer and no fibre damage was recorded in the skin. The second major failure observed is skin/stringer separation. The delaminated surfaces remain within the interface between skin and stiffener and crack jumping is not apparent. In order to predict the damage initiation load and mode, the 3D stress fields obtained by the UF-SLE model, at various load levels in the post-buckling regime, are plugged in the Hashin 3D failure criteria [34] for the prediction of ply failure, and in the mixed mode quadratic criteria [35] to determine the onset of delamination. The failure indices are calculated using the stress state in the material coordinate system (1,2,3) by:

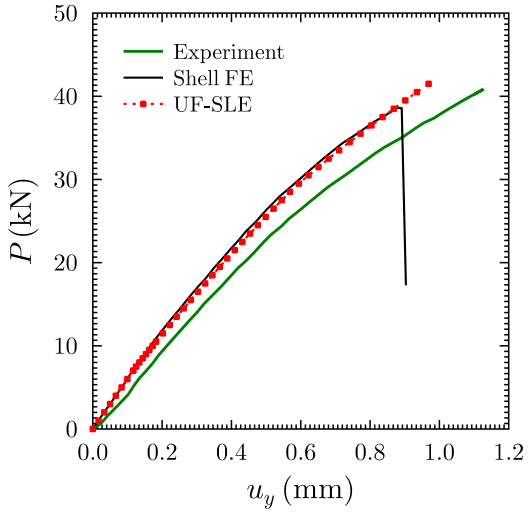

Figure 12: Load-displacement curve for the single-stringer composite panel subjected to compression. Experiment and Shell FE results are taken from [31].

1. Fibre Tension for $\sigma_{11} \geq 0$:

$$\left(\frac{\sigma_{11}}{ST_{11}}\right)^2 + \left(\frac{\sigma_{12}^2 + \sigma_{13}^2}{SS_{12}^2}\right) \geq 1, \tag{25}$$

2. Fibre Compression for $\sigma_{11} < 0$:

$$\left(\frac{\sigma_{11}}{SC_{11}}\right)^2 \geq 1, \tag{26}$$

3. Matrix Tension for $\sigma_{22} + \sigma_{33} \geq 0$:

$$\left(\frac{\sigma_{22} + \sigma_{33}}{ST_{22}}\right)^2 + \left(\frac{\sigma_{23}^2 - \sigma_{22}\sigma_{33}}{SS_{23}^2}\right) + \left(\frac{\sigma_{12}^2 + \sigma_{13}^2}{SS_{12}^2}\right) \geq 1, \tag{27}$$

4. Matrix Compression for $\sigma_{22} + \sigma_{33} < 0$:

$$\left[\left(\frac{SC_{22}}{2SS_{23}}\right)^2 - 1\right]\left(\frac{\sigma_{22} + \sigma_{33}}{SC_{22}}\right) + \left(\frac{\sigma_{22} + \sigma_{33}}{2SS_{23}}\right)^2 + \left(\frac{\sigma_{23}^2 - \sigma_{22}\sigma_{33}}{SS_{23}^2}\right) + \left(\frac{\sigma_{12}^2 + \sigma_{13}^2}{SS_{12}^2}\right) \geq 1, \tag{28}$$

5. Delamination for $\sigma_{33} \geq 0$:

$$\left(\frac{\sigma_{33}}{ST_{33}}\right)^2 + \left(\frac{\sigma_{23}}{SS_{33}}\right)^2 + \left(\frac{\sigma_{13}}{SS_{33}}\right)^2 \geq 1, \tag{29}$$

where ST, SC and SS denotes tensile strength, compressive strength and shear strength of the material, σ_{ij} terms denote the components of the stress tensor in the material coordinate system, and subscripts 1, 2 and 3 represents the fibre direction, the in-plane direction orthogonal to fibres, and the direction normal to the layer plane, respectively.

The intralaminar damage of the fibre and the matrix is evaluated in terms of failure indices using Eqs. (25) to (28). It is observed that at a load level of 36 kN, transverse tension and in-plane shear cause

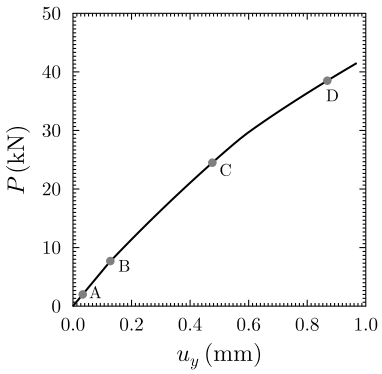

(a) Load-axial displacement curve predicted by the UF-SLE model.

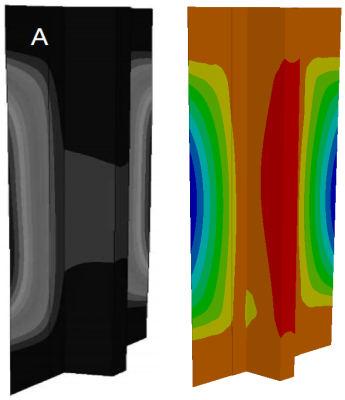

(b) Response predicted at 2 kN. Shell FE (left) and UF-SLE (right)

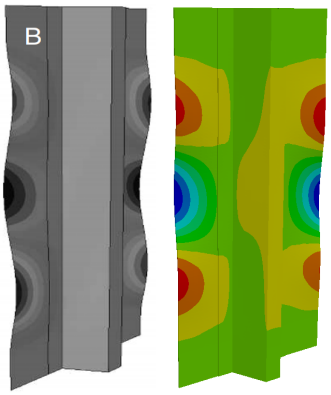

(c) Skin buckling: 7.5 kN (Shell FE, left) and 7.8 kN (UF-SLE, right)

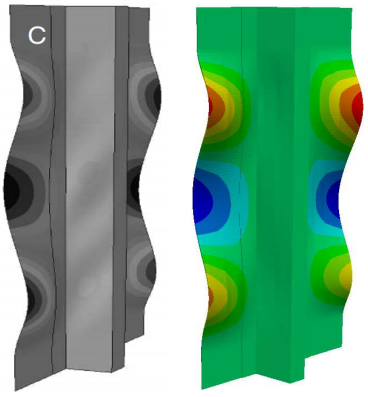

(d) Stringer buckling: 23.5 kN (Shell FE, left) and 24.5 kN (UF-SLE, right)

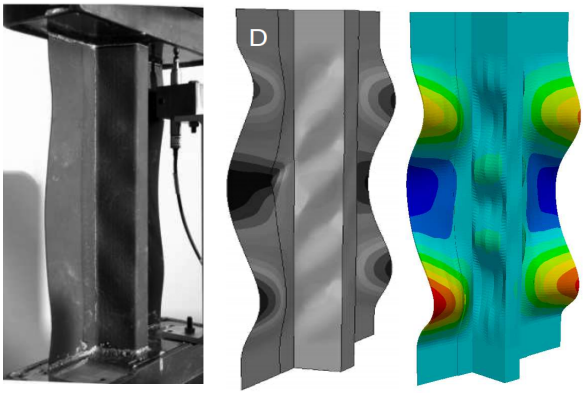

(e) Before collapse: 41 kN (Experiment, left), 39 kN (Shell FE, centre) and 39.5 kN (UF-SLE, right)

Figure 13: Out of plane displacement response predicted by the UF-SLE model at different load levels compared to those obtained by the Shell FE model and Experiment [31].

matrix cracking at different locations along the stringer. Although, transverse matrix cracking is considered as the benign mode of failure, that corresponds to a small reduction in the overall stiffness of the structure which can affect the evolution of damage. However, the present model does not account for any degradation in the material stiffness property, and is used herein for first-ply failure analysis. With a further increase in applied load, the areas with matrix damage become more extensive and starts to extend into the skin. At a load level of 39.5 kN, fibre damage initiation is observed and fractures are predicted at the corners between the stringer webs and the corresponding flanges, as shown in Figure 14c. Also, the matrix damage contour is shown in Figure 14d which is highly diffused. These failure contour plots indicate fibre-matrix debonding at discrete locations along the stringer, which can further cause fibre pullouts in these regions as was observed in the experiment.

The transverse stress fields obtained by the UF-SLE model are used for predicting the onset of delamination using Eq. (29). Figure 14e shows the delamination index contour obtained at the applied load of 39.5 kN. From the contour plot, the skin and the stringer separation (red fringe) is likely to initiate from: (i) two different locations along the length, at the stringer flange and skin interface, present on either side of the stringer; and (ii) from the the mid-length in the region around the stringer web and flange junction. This delamination prediction by the present model is in close agreement with experiments. Although, with current capabilities and using 3D stress fields, it is difficult to predict the crippling fracture of the specimen as its accurate prediction requires progressive failure models.

To conclude it is important to remark on the computational efficiency of the UF-SLE model compared to the reference shell FE model, which can be estimated by comparing the degrees of freedom required for convergence. The approximate number of DOFs required by the shell model is 710,000, which is three times more than that required by the present model. Moreover, unlike shell elements, Serendipity Lagrange elements are capable of predicting 3D stress fields. In contrast, obtaining 3D stress fields using a FE model require brick elements, and solving such high-fidelity model is cumbersome and expensive. Thus, the proposed model offers significant computational benefit, over shell FE model, together with solid-like FE capabilities.

4. Conclusions

Previous studies [20, 21, 23, 36, 37] highlighted the ability of the Unified Formulation, based on Serendipity Lagrange expansions (UF-SLE), to capture localised three-dimensional (3D) stress fields accurately, in isotropic, constant- and variable-stiffness, laminated composite and sandwich structures. The hierarchical nature of the Serendipity Lagrange expansions allows the fidelity of the model to be tuned, such that low-fidelity and high-fidelity models can be used concurrently to assess global response and 3D stresses. In this work, geometric nonlinear modelling capabilites are incorporated within the UF-SLE model and then employed for the large deflection analysis of isotropic and laminated composite structures. The nonlinear governing equations and the finite element approximation are formulated using the principle of virtual work. All classical material stiffness terms are considered in the formulation, thereby making it complete and suitable for analysing fully anisotropic structures. The explicit form of the tangent stiffness matrix, in terms of the fundamental nuclei, is provided in a clear concise notation and the benefit of writing these expressions in such a way is discussed. These expressions are general, meaning they can be adapted, as they are independent of the expansion function used in the cross-section, within the Unified Formulation framework. The nonlinear structural response obtained by the UF-SLE model is shown to match experimental data, shell and solid Finite Element (FE) solutions and numerical results available in the literature. The nonlinear 3D stress fields, evaluated using the present model, are used for predicting damage initiation in a stiffened composite structure subjected to compression. The results indicate a good correlation with experimental data in terms of load-displacement response in the pre- and post-buckling range. The model also offers insight on the intralaminar failure mechanisms and correctly predicts the initiation of the separation of the skin from the stringer as obtained experimentally. Finally, the proposed model offers computational benefits over conventional FE models, while maintaining similar levels of accuracy. This study provides confidence in using advanced damage modelling capabilities within the present formulation, and together with its efficiency and accurate stress predicting capability, can be a useful tool for structural analysis.

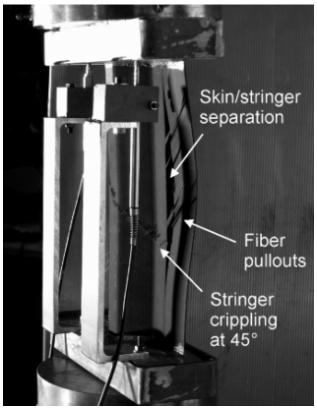

(a) Experimental failure mode

(b) Experimental collapse mode

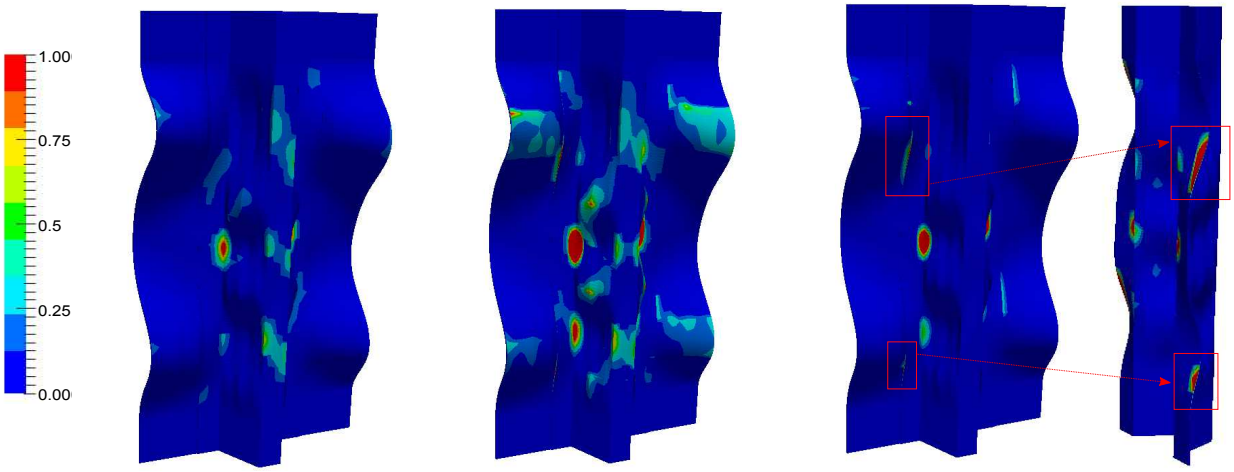

(c) Fibre damage

(d) Matrix damage

(e) Onset of delamination

Figure 14: Experimental [31] and predicted numerical failure modes of a single-stringer composite panel.

Acknowledgements

This research has been developed in the framework of the FULLCOMP project, supported by the H2020 Marie Skłodowska-Curie European Training Network [Grant No. 642121]. Mayank Patni and Sergio Minera would like to thank Aerospace Structures and Materials (ASM) department at Delft University of Technology for hosting them in the spring of 2018. Alberto Pirrera is funded by the EPSRC [Grant No. EP/M013170/1]. Paul M. Weaver would like to acknowledge the support of the Royal Society for the Royal Society Wolfson Merit and the Science Foundation Ireland for the award of a Research Professor grant (Varicomp: 15/RP/2773).

Data Statement

All data required to reproduce the figures in this paper can be found on the data repository of the University of Bristol via URL: http://data.bris.ac.uk/data/.

References

[1] R. Vescovini, C. G. Dávila, C. Bisagni, Failure analysis of composite multi-stringer panels using simplified models, Composites Part B: Engineering 45 (2013) 939–951.
[2] M. J. Hinton, P. D. Soden, Failure criteria for composite laminates, Composite Science and Technology 58 (1998) 1001–1010.
[3] J. N. Reddy, A. K. Pandey, A first-ply failure analysis of composite laminate, Composite Structures 25 (1987) 371–393.
[4] Y. S. N. Reddy, J. N. Reddy, Linear and non-linear failure analysis of composite laminates with transverse shear, Composite Science and Technology 44 (1992) 227–255.
[5] Y. S. N. Reddy, J. N. Reddy, Three-dimensional finite element progressive failure analysis of composite laminates under axial extension, Journal of Composite Technology 15 (1993) 73–87.
[6] P. Maimí, P. P. Camanho, J. A. Mayugo, C. G. Dávila, A continuum damage model for composite laminates: Part I – Constitutive model, Mechanics of Materials 39 (2007) 897–908.
[7] G. Catalanotti, P. P. Camanho, A. T. Marques, Three-dimensional failure criteria for fiber-reinforced laminates, Composite Structures 95 (2013) 63–79.
[8] M. Meng, H. R. Le, M. J. Rizvi, S. M. Grove, 3D FEA modelling of laminated composites in bending and their failure mechanisms, Composite Structures 119 (2015) 693–708.
[9] N. S. Putcha, J. N. Reddy, A refined mixed shear flexible finite element for the nonlinear analysis of laminated plates, Computers and Structures 22 (1986) 529–538.
[10] E. J. Barbero, J. N. Reddy, Nonlinear analysis of composite laminates using a generalized laminated plate theory, AIAA Journal 28 (1990) 1987–1994.
[11] K. Lee, S. W. Lee, A postprocessing approach to determine transverse stresses in geometrically nonlinear composite and sandwich structures, Journal of Composite Material 37 (2003) 2207–2224.
[12] Y. X. Zhang, K. S. Kim, A simple displacement-based 3-node triangular element for linear and geometrically nonlinear analysis of laminated composite plates, Computational Methods in Applied Mechanics 194 (2005) 4607–4632.
[13] Y. X. Zhang, C. H. Yang, Recent developments in finite element analysis for laminated composite plates, Composite Structures 88 (2009) 147–157.
[14] E. Carrera, M. Cinefra, M. Petrolo, E. Zappino, Finite Element Analysis of Structures through Unified Formulation, Wiley, Politecnico di Torino, Italy, 2014.
[15] E. Carrera, G. Giunta, M. Petrolo, A Modern and Compact Way to Formulate Classical and Advanced Beam Theories, Saxe-Coburg Publications, United Kingdom, 2010.
[16] A. G. de Miguel, I. Kaleel, M. H. Nagaraj, A. Pagani, M. Petrolo, E. Carrera, Accurate evaluation of failure indices of composite layered structures via various FE models, Composites Science and Technology 167 (2018) 174–189.
[17] A. Pagani, E. Carrera, Large-deflection and post-buckling analyses of laminated composite beams by Carrera Unified Formulation, Composite Structures 170 (2017) 40 – 52.
[18] A. Pagani, E. Carrera, Unified formulation of geometrically nonlinear refined beam theories, Mechanics of Advanced Materials and Structures 25 (1) (2018) 15 – 31.
[19] Y. Hui, G. D. Pietro, G. Giunta, S. Belouettar, H. Hu, E. Carrera, A. Pagani, Geometrically nonlinear analysis of beam structures via hierarchical one-dimensional finite elements, Mathematical Problems in Engineering 2018 (2018) 1–22.
[20] S. Minera, M. Patni, E. Carrera, M. Petrolo, P. M. Weaver, A. Pirrera, Three-dimensional stress analysis for beam-like structures using serendipity lagrange shape functions, International Journal of Solids and Structures 141-142 (2018) 279 – 296.
[21] M. Patni, S. Minera, R. M. J. Groh, A. Pirrera, P. M. Weaver, Three-dimensional stress analysis for laminated composite and sandwich structures, Composites Part B: Engineering 155 (2018) 299–328.
[22] S. O. Ojo, M. Patni, P. M. Weaver, Comparison of weak and strong formulations for the 3D stress predictions of composite beam structures, Submitted to International Journal of Solids and Structures.

[23] M. Patni, S. Minera, R. M. J. Groh, A. Pirrera, P. M. Weaver, On the accuracy of localised 3D stress fields in tow-steered laminated composite structures, Composite Structuresdoi:doi.org/10.1016/j.compstruct.2019.111034.
[24] M. A. Crisfield, J. J. Remmers, C. V. Verhoosel, et al., Nonlinear finite element analysis of solids and structures, John Wiley & Sons, 2012.
[25] K. J. Bathe, Finite Element Procedures, Prentice-Hall, Inc., USA, 1996.
[26] J. N. Reddy, An Introduction to Nonlinear Finite Element Analysis, Second Edition, Oxford University Press, UK, 2015.
[27] A. Hoger, D. E. Carlson, Determination of the stretch and rotation in the polar decomposition of the deformation gradient, Quarterly of Applied Mathematics 42 (1984) 113 – 117.
[28] K. E. Bisshopp, D. C. Drucker, Large deflection of cantilever beams, Quarterly of Applied Mathematics 3 (1945) 272–275.
[29] J. D. Kemper, Large deflections of tapered cantilever beams, International Journal of Mechanical Sciences 10 (6) (1968) 469 – 478.
[30] G. S. Payette, J. N. Reddy, A seven-parameter spectral/hp finite element formulation for isotropic, laminated composite and functionally graded shell structures, Computer Methods in Applied Mechanics and Engineering 278 (2014) 664 – 704.
[31] C. Bisagni, R. Vescovini, C. G. Dávila, Single-stringer compression specimen for the assessment of damage tolerance of postbuckled structures, Journal of Aircraft 48 (2011) 495–502.
[32] C. Bisagni, C. G. Dávila, Experimental investigation of the postbuckling response and collapse of a single-stringer specimen, Composite Structures 108 (2014) 493–503.
[33] C. C. Chamis, F. Abdi, M. Garg, L. Minnetyan, H. Baid, D. Huang, J. Housner, F. Talagani, Micromechanics-based progressive failure analysis prediction for WWFE-III composite coupon test cases, Journal of Composite Materials 47 (2013) 2695–2712.
[34] Z. Hashin, Failure criteria for unidirectional fiber composites, Journal of Applied Mechanics 47 (1980) 329–334.
[35] J. C. Brewer, P. A. Lagace, Quadratic stress criterion for initiation of delamination, Journal of Composite Materials 22 (1988) 1141–1155.
[36] M. Patni, S. Minera, P. M. Weaver, A. Pirrera, A computationally efficient model for three-dimensional stress analysis of stiffened curved panels, In Proceedings of the International Conference on Composite Materials and Structures, ICCMS 2017, Hyderabad, India - (2017) 1–12.
[37] M. Patni, S. Minera, R. M. J. Groh, A. Pirrera, P. M. Weaver, Efficient 3d stress capture of variable stiffness and sandwich beam structures, AIAA Scitech 2019 Forumdoi:doi.org/10.2514/6.2019-1763.